Methods 253 (2026) 19–30

Contents lists available at ScienceDirect

Methods

journal homepage: www.elsevier.com/locate/ymeth

TEAMSTER: End-to-end pipeline for generation, processing, and automated quantitative image analysis of 3D tumour spheroids for nanobiology☆

Linda Barbieri [a,b,1], Andrea Banfi [a,1], Stefania Garbujo [a,b], Lucia Salvioni [a,b], Chiara Baioni [a], Giulia Tomaino [a], Maria Rita Chelazzi [a], Luisa Fiandra [a], Miriam Colombo [a,b], Davide Prosperi [a,b,*,2], Metello Innocenti [a,*,2]

[a] Department of Biotechnology and Bioscience, University of Milano-Bicocca, Piazza della Scienza 2, 20126 Milano, Italy
[b] Nanomedicine Center NANOMIB, University of Milan-Bicocca, Milan, Italy

ARTICLE INFO

Keywords:
Tumour spheroids
Image analysis
3D cultures

ABSTRACT

Three-dimensional (3D) tumour spheroids are widely used as physiologically relevant in vitro models to study tumour biology, therapeutic responses, and the distribution of drugs and nanomaterials. However, experimental workflows for spheroid-based studies remain highly heterogeneous, with limited standardization across spheroid generation, processing, and quantitative analysis, hindering reproducibility and accessibility. Here, we present TEAMSTER, an integrated, end-to-end pipeline for the generation, cryosectioning, immunostaining, and quantitative image analysis of tumour spheroids. The workflow combines optimized protocols for reproducible spheroid formation that minimize variability, a liquid nitrogen-free, colour-coded OCT embedding strategy improving spheroid localization during cryosectioning, standardized fixation and staining procedures compatible with multiplex fluorescence imaging, and a semi-automated, GUI-based CellProfiler pipeline enabling unbiased quantitative analysis without coding skills, machine learning, or dedicated computing hardware. TEAMSTER is experimentally validated in two distinct tumour spheroid models treated with fluorescently labelled nanoconjugates. Quantitative performance metrics for spheroid preparation (intraplate and interplate coefficients of variation) and image segmentation benchmarking (Dice and IoU coefficients) support the robustness of single-cell-resolved measurements across cryosectioned spheroid models and imaging conditions. By prioritizing experimental robustness, standardization, and usability, TEAMSTER provides a practical methodological resource for reproducible quantitative spheroid-based studies in cancer biology and nanomedicine.

1. Introduction

The transition from two-dimensional (2D) to three-dimensional (3D) cell culture models has represented a major methodological advance in cancer research, enabling experimental systems with improved physiological relevance. By permitting cell–cell and cell-matrix interactions, spatial organization, and the formation of diffusion gradients, 3D models more closely recapitulate key features of the tumour microenvironment (TME) than conventional 2D cultures. As a result, tumour spheroids are now widely used to investigate tumour biology, assess therapeutic efficacy, and evaluate the penetration and distribution of drugs and nanomaterials. [1,2].

Among available 3D systems, tumour spheroids offer a tractable and scalable model that can be generated using either scaffold-based or scaffold-free approaches. Scaffold-based methods rely on extracellular matrix (ECM) components of biological origin, such as basement membrane extracts, or synthetic hydrogels engineered to mimic key ECM properties [3–5], whereas scaffold-free approaches exploit the intrinsic ability of tumour cells to self-aggregate under non-adhesive conditions, including hanging-drop cultures, rotational systems, and low-adhesion multiwell plates. [6] Spheroid size can be precisely controlled by the number of seeded cells, and spheroids exceeding approximately 400 μm in diameter develop gradients of oxygen and nutrients that give rise to spatially organized proliferative, quiescent,

☆ This article is part of a special issue entitled: 'Editors Collection - YMETH' published in Methods.

* Corresponding authors.
E-mail addresses: davide.prosperi@unimib.it (D. Prosperi), metello.innocenti@unimib.it (M. Innocenti).

[1] Co-first.
[2] Co-corresponding.

https://doi.org/10.1016/j.ymeth.2026.04.015
Received 15 December 2025; Received in revised form 30 March 2026; Accepted 29 April 2026
Available online 6 May 2026

and necrotic regions, closely resembling those observed in solid tumours. [1,7]

Tumour spheroids can be generated from established cell lines or derived directly from tumour samples, offering flexibility in modelling. When embedded within ECM-based scaffolds, spheroids form hybrid culture systems that combine the structural support of scaffold-based methods with the physiological relevance of spheroid formation, thus enhancing the ability to replicate the complex TME *in vitro*. [4,8–10]

Despite these advantages and their widespread adoption, available experimental workflows for spheroid formation are highly heterogeneous, and downstream processing steps, including fixation, cryosectioning, immunostaining, and quantitative image analysis, are often insufficiently standardized. In particular, spheroid handling during embedding and sectioning is prone to sample loss and deformation, immunostaining procedures frequently yield variable signal-to-noise ratios, and image analysis commonly relies on manual workflows or computational tools requiring advanced expertise and infrastructure. Together, these limitations compromise reproducibility, reduce quantitative robustness, and restrict the accessibility of spheroid-based assays. Although recent studies have addressed selected aspects of spheroid processing and imaging, including whole-mount staining and automated confocal imaging [11], cryosectioning and antigen-retrieval procedures [12], mold-based systems for spheroid and microtissue formation [13], workflows comparing whole-mount and section-based strategies [14], and deep-learning-based image analysis [15], these advances have generally been developed for specific applications and do not provide a broadly accessible integrated solution.

To address these challenges, we developed TEAMSTER, an experimentally validated end-to-end workflow for tumour spheroid generation, processing, and quantitative analysis. TEAMSTER integrates reproducible spheroid formation, improved cryo-embedding and sectioning, standardized multiplex-compatible immunostaining, and a semi-automated GUI-based CellProfiler pipeline for unbiased quantitative image analysis. Importantly, this workflow enables robust single-cell-resolved measurements supported by quantitative performance metrics without requiring coding skills, machine learning approaches, or dedicated computing hardware. By prioritizing standardization, experimental robustness, and usability, TEAMSTER provides a broadly applicable methodological resource for reproducible quantitative spheroid-based studies in cancer biology and nanomedicine.

2. Materials and methods

2.1. Spheroid formation and CV calculation

U-87 MG glioblastoma cells and MDA-MB-231 triple negative breast cancer cells were used to showcase ECM-independent and ECM-dependent spheroid formation respectively. Cells were seeded into ultra-low attachment 96-well plates and centrifuged at 320xg for 10 min using an Eppendorf 5810 centrifuge (Eppendorf AG, Hamburg) to promote uniform aggregation. For ECM-dependent cultures, Cultrex® basement membrane extract (3-D Culture Matrix Reduced Growth Factor BME, R&D System) was included to enhance structural integrity. Spheroids were cultured for 5 days prior to downstream processing (Supplementary method S1). Intra- and inter-plate coefficients of variation were calculated using the following formulas:

CV intraplate (%) = (SD of mean intraplate volume/mean intraplate volume) x 100

CV interpolate (%) = (SD of mean interplate volume/mean interplate volume) x 100

2.2. Treatment with compounds

Spheroids were treated at day 5 of culture. After carefully removing the culture medium, two washes with PBS were performed prior to adding HFn-CTX nanoconjugate labelled with AlexaFluor-647 and AlexaFluor-750, respectively, diluted in complete medium (Supplementary method S2).

2.3. Fixation and embedding in OCT

Spheroids were first fixed in pre-warmed 4% paraformaldehyde (PFA) in PEM buffer for 2 hours at room temperature (RT). [16,17] After fixation, they were washed once with PBS and subsequently dehydrated by incubation in 30% sucrose for 2 hours at RT. To facilitate sectioning and easy identification of spheroids, a layered colour-coded OCT embedding approach was used (see below). Spheroids were embedded in optimal cutting temperature (OCT) compound, a water-soluble, polymer-based medium commonly used for frozen histology and immunofluorescence. OCT was selected because it provides mechanical support during freezing and cryosectioning, facilitates handling of small and delicate 3D samples, helps preserve overall spheroid architecture, and is compatible with downstream fluorescence staining with limited background (Supplementary method S3). Before sectioning, OCT-embedded spheroids were left at -20 °C for at least 1 h or better overnight to soften. Cryosections (7 μm) were collected on SuperFrost Plus slides and air-dried before storage or further processing (Supplementary method S4).

2.4. Immunostaining and image acquisition

First a Dako pen was used to circle the spheroid on the slide. Then, sections were permeabilized, blocked, and stained with primary and secondary antibodies alongside nuclear markers as previously described. [18] Coverslips were mounted using an antifade reagent (FluorSave Reagent, Millipore Corporation) (Supplementary method S5). Imaging was performed using a Leica Thunder Imager fluorescence microscope under identical acquisition settings for all samples. Images were captured using a 63X/1.4 oil immersion objective and at 16-bit depth, with dimensions ranging between 1900 and 3800 pixels (corresponding to 390 and 780 μm, respectively) (Supplementary method S6).

Inclusion and exclusion criteria were defined prior to analysis as follows: images were included only if they contained a clearly identifiable spheroid cross-section that was intact and undamaged. Images were excluded if they showed folded or physically compromised tissue sections, if no distinguishable spheroid cross-section could be identified, or if obvious technical artifacts were present that could interfere with accurate assessment. These criteria were applied consistently across all samples to ensure that only images of sufficient quality and morphological clarity were retained for downstream analysis.

2.5. Image analysis using CellProfiler

CellProfiler (version 4.2.8) [19] was employed to quantify the distribution of fluorescent nanoparticles within cryosectioned tumour spheroids, as well as morphometric parameters thereof. A bespoke pipeline (Supplementary file TEAMSTER CellProfiler pipeline) was designed to perform standardized image loading, object identification, and intensity-based quantification of fluorescent signals, allowing robust automated analyses without the need for coding expertise.

In brief, images were subjected to object segmentation using intensity-based thresholding. Each spheroid was identified as a discrete object starting from cell nuclei, which were counted and profiled for their morphometric parameters, generating a mask from which several fluorescence intensity measurements were extracted (Supplementary method S7). Altogether, these metrics enabled robust, per-spheroid quantification of nanoparticle uptake across experimental conditions. Additionally, morphological descriptors (e.g., area, eccentricity, number and distribution of nuclei) were recorded to characterize spheroids and assess their uniformity, maximizing consistency across sample preparations and treatments. A reference image dataset for the pipeline is provided. Although the pipeline is very robust, some tweaking might be

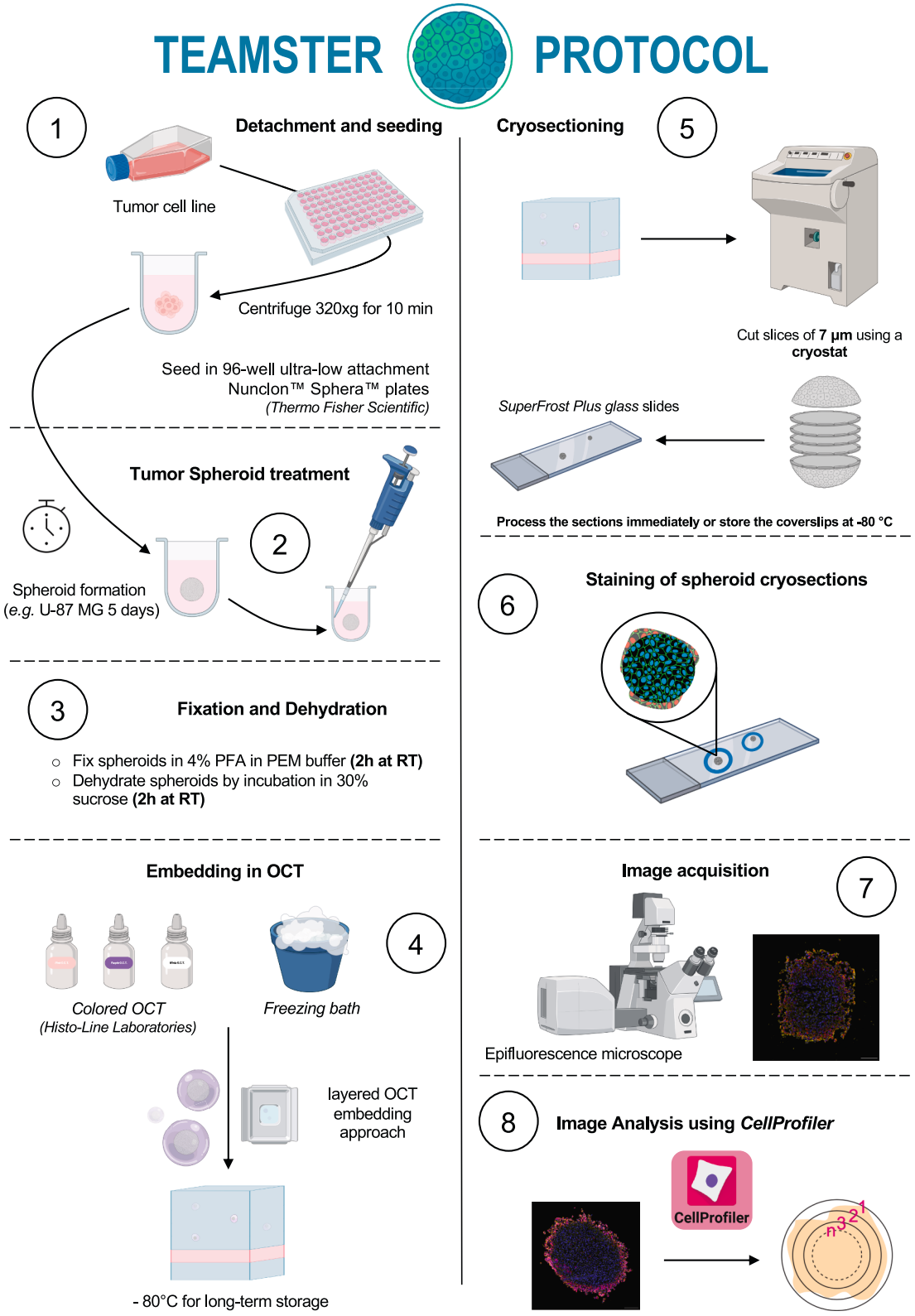

Fig. 1. Overview of TEAMSTER. Stepwise schematic of TEAMSTER illustrating its modular structure, from spheroid generation to automated image analysis. Tumour cells are seeded in ultra-low attachment plates to promote reproducible 3D spheroid formation (step 1), followed by optional treatment with compounds or nanoparticle formulations (step 2). Spheroids are fixed and dehydrated in sucrose (step 3) before embedding in a layered, colour-coded OCT block to enhance localization during cryosectioning (step 4). Thin sections (7 µm) are collected onto SuperFrost Plus slides (step 5) and processed for multiplex fluorescence staining (step 6). High-resolution images are acquired using an epifluorescence microscope under standardized conditions (step 7) and quantitatively analysed leveraging an unbiased GUI-based CellProfiler pipeline (step 8). The modularity of TEAMSTER allows adaptation to diverse 3D models, staining panels, and imaging modalities.

A.

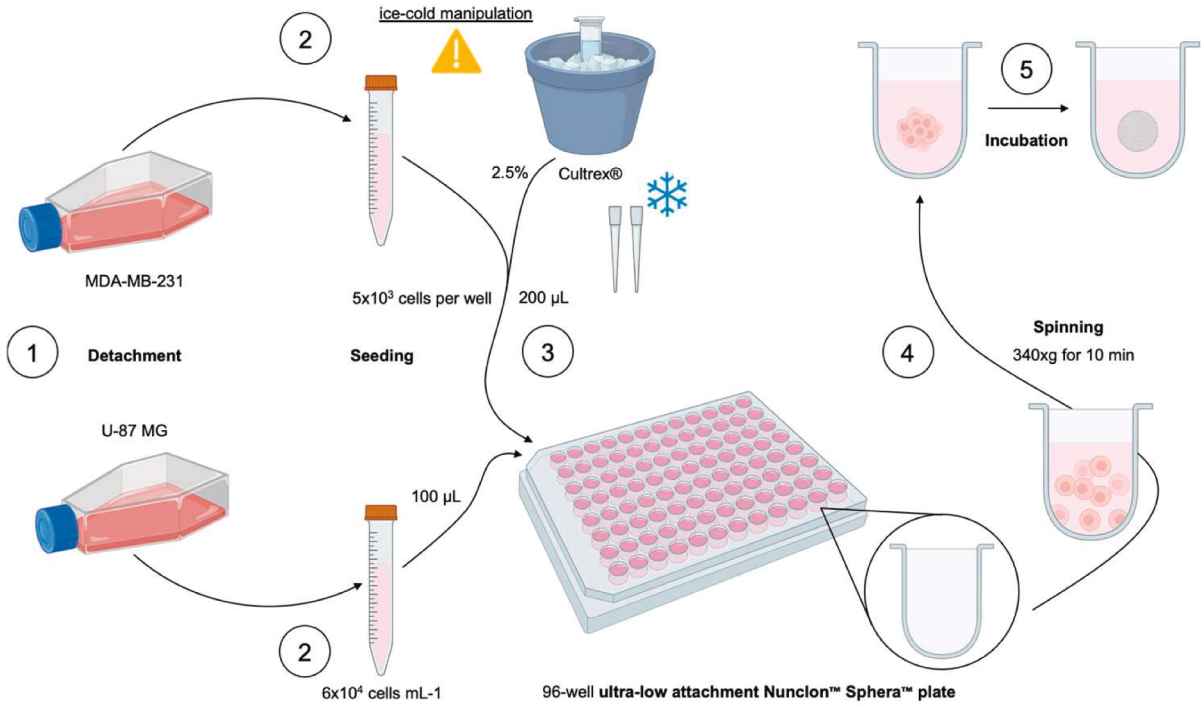

B.

U-87 MG	Number of spheroids	CV% intraplate	CV% interplate
exp 1	12	7.88	8.9
exp 2	12	5.89	
exp 3	20	4.83	

MDA-MB-231	Number of spheroids	CV% intraplate	CV% interplate
exp 1	12	3.97	9.4
exp 2	11	8.69	
exp 3	8	4.17	

Fig. 2. Protocol for spheroids production. A) Schematic representation of the workflow followed to obtain U-87 MG and MDA-MB-231 spheroids. B) Intraplate and interplate coefficients of variation (CV%) for U-87 MG and MDA-MB-231 spheroids.

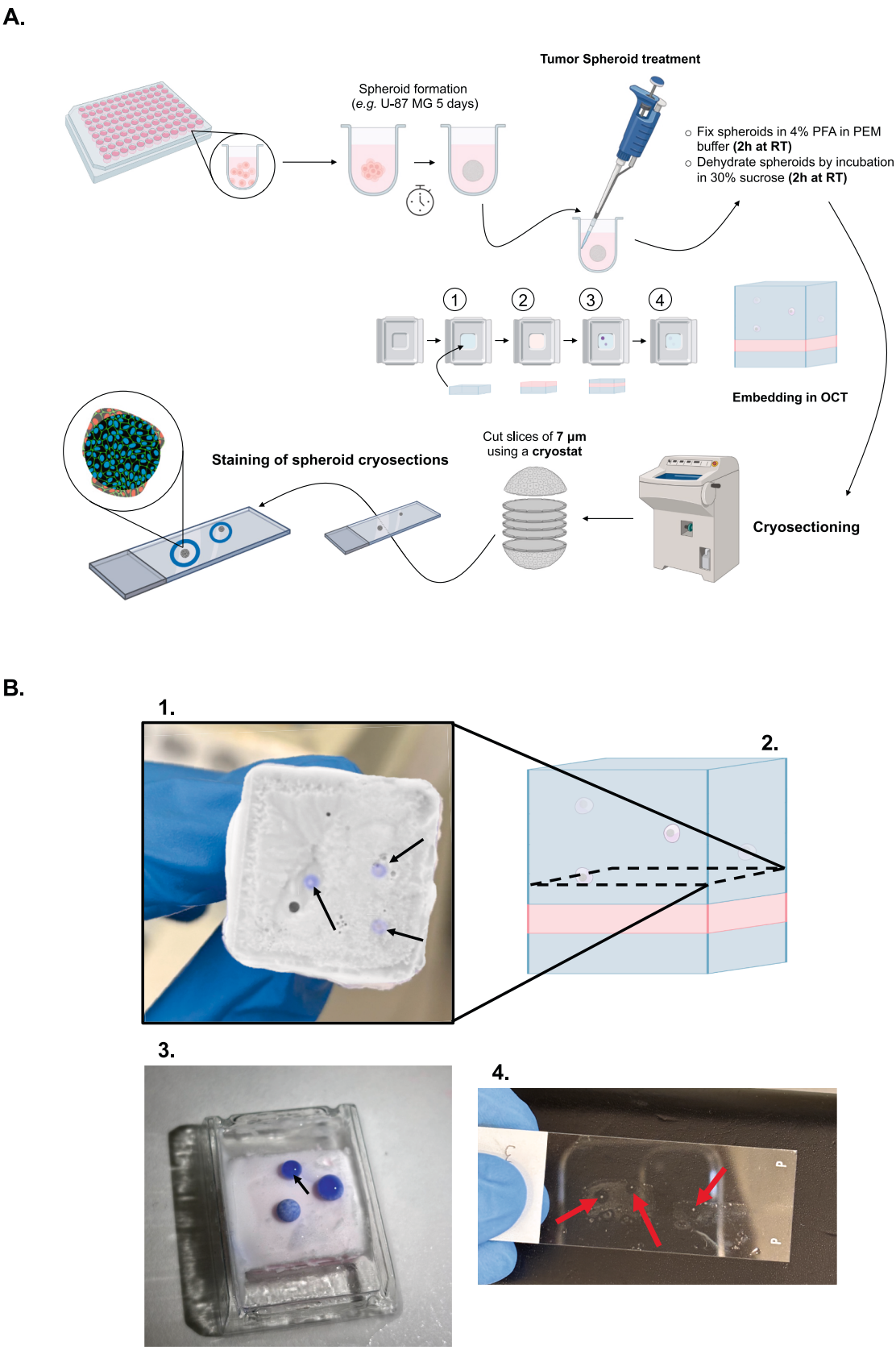

Fig. 3. Color-coded OCT embedding strategy for improved spheroid localization during cryosectioning. A) Schematic representation of the steps required to obtain spheroid cryosections. B) Representative images of the layered OCT embedding approach used in TEAMSTER. (1) OCT block containing tumour spheroids (arrows) embedded between alternating transparent and pigmented OCT layers. (2) Schematic illustration of the embedding principle, where the colored OCT provides a visual landmark to identify the spheroid plane during sectioning (dashed line). (3) OCT block after solidification showing spheroids embedded at a defined interface. (4) Cryosection collected on a SuperFrost Plus slide, with arrows indicating spheroids successfully retrieved.

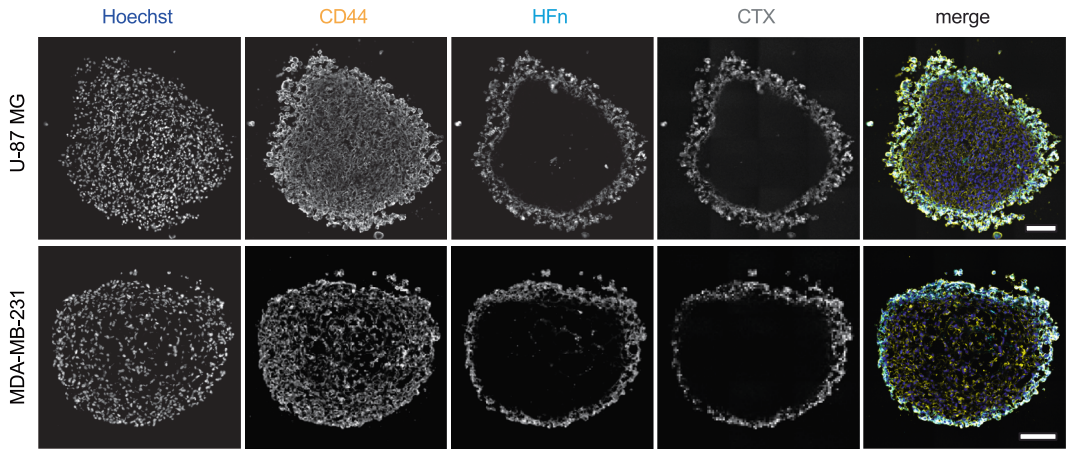

Fig. 4. Nanoconjugate distribution in glioblastoma and TNBC spheroids. Representative cryosections of U-87 MG and MDA-MB-231 spheroids incubated with double labelled HFn-CTX (0.1 mg mL^{-1} each) for 30 min. Plasma membrane stained with CD44 is depicted in yellow, nuclei stained with Hoechst in blue, HFn-AF647 (HFn) in cyan, CTX-AF750 (CTX) in grey in the merged image.

needed when the quality of the staining or image resolution and dynamic range greatly differ from ours, as recommended elsewhere (https://tutorials.cellprofiler.org/).

2.6. Segmentation benchmarking and object-level validation

To assess segmentation performance and single-cell identification accuracy, a small benchmarking dataset was generated from 6 representative cryosection images of U-87 MG and MDA-MB-231 spheroids. For each image, three segmentation outputs were compared: the TEAMSTER CellProfiler-based pipeline, the Cellpose Cyto3 model, and the Cellpose nuclei model. For the latter two models, images were opened and calibrated in Cellpose before segmentation. Manual ground-truth (GT) annotations were generated for the same images and used as the reference for all comparisons.

For pixel-level benchmarking, binary masks were produced for each method and for the corresponding manual GT annotation. Masks were exported as grayscale TIFF images of identical size and spatial registration, with foreground pixels corresponding to segmented nuclei and background pixels corresponding to non-nuclear areas. Before metric calculation, all masks were converted to 8-bit binary images, and all pixels with intensity greater than 0 were considered positive pixels.

Segmentation accuracy was quantified using the Dice coefficient and the intersection-over-union (IoU), calculated by comparing each predicted mask against the corresponding GT mask.

The Dice coefficient was calculated as follows: $\text{Dice} = 2 \times |A \cap B| / (|A| + |B|)$, where A is the set of positive pixels in the GT mask, B is the set of positive pixels in the predicted mask, $|A \cap B|$ is the number of overlapping positive pixels, and $|A|$ and $|B|$ are the total numbers of positive pixels in the GT and predicted masks, respectively.

The IoU was calculated as follows: $\text{IoU} = |A \cap B| / |A \cup B|$, where $|A \cup B|$ is the number of pixels belonging to the union of the GT and predicted masks. A Dice or IoU value of 1 indicates perfect overlap between the predicted and GT masks, whereas lower values indicate lower segmentation agreement.

Dice and IoU were determined using a custom Fiji/ImageJ macro developed for this study. Briefly, the macro imported the GT and predicted masks for each image pair, converted them to 8-bit binary masks using a threshold of pixel intensity > 0, and verified that both masks had identical dimensions. The intersection between masks was computed using the Image Calculator "AND" operation, and the union was computed using the "OR" operation. The numbers of positive pixels in the individual masks, intersection mask, and union mask were extracted from the pixel histograms and used to calculate Dice and IoU according to the formulas above. The macro processed all image triplets in batch mode and exported both per-image and summary results to a tab-separated output file.

The number of nuclei identified by each method was compared against manual GT counts. For each benchmark image, the absolute counting error was calculated as follows: Absolute error $= |\text{Npred} - \text{NGT}|$, where Npred is the number of nuclei identified by the tested method and NGT is the corresponding manual GT count.

To normalize counting error across images with different total cell numbers, the percent counting error was also calculated using the following formula: Percent error $= (|\text{Npred} - \text{NGT}| / \text{NGT}) \times 100$.

For each method, overall counting performance was summarized using the mean absolute error (MAE), defined as $\text{MAE} = (1/n) \times \Sigma\, |\text{Npred,i} - \text{NGT,i}|$, where n is the number of benchmark images. Mean percent error was calculated analogously as the arithmetic mean of percent counting errors across all images.

Full experimental details, reagent lists, step-by-step protocols, and a video showing how to use a cryostat are provided as **Supplementary material**.

3. Results

3.1. Integrated pipeline for 3D tumour spheroids analysis

TEAMSTER offers a user-friendly pipeline for the generation, processing, and quantitative image analysis of 3D tumour spheroids. It details, step by step, a series of optimized up-to-date procedures needed to achieve this objective (Fig. 1). First, a customizable protocol to obtain tumour spheroids, with or without ECM components. Second, a safe snap-freezing procedure for spheroid embedding that avoids liquid nitrogen and improves spheroid findability through a novel colour-coded optimal cutting temperature compound (OCT) embedding strategy. Third, an optimized immunostaining for high signal-to-noise fluorescence imaging, and fourth a semi-automated GUI-based image analysis pipeline using CellProfiler.

3.2. Standardized and reproducible tumour spheroid production

For spheroids to serve as truly physiologically relevant models, their generation must follow harmonised procedures that yield consistent morphometric and functional readouts across experiments and laboratories. Recent technical advances, now widely adopted, have enabled the attainment of satisfactory intra-plate and inter-plate coefficients of variation (CVs) for U-87 MG glioblastoma spheroid volume, approximately 7% and 18%, respectively. [20]

We asked whether this variability could be reduced even further. By

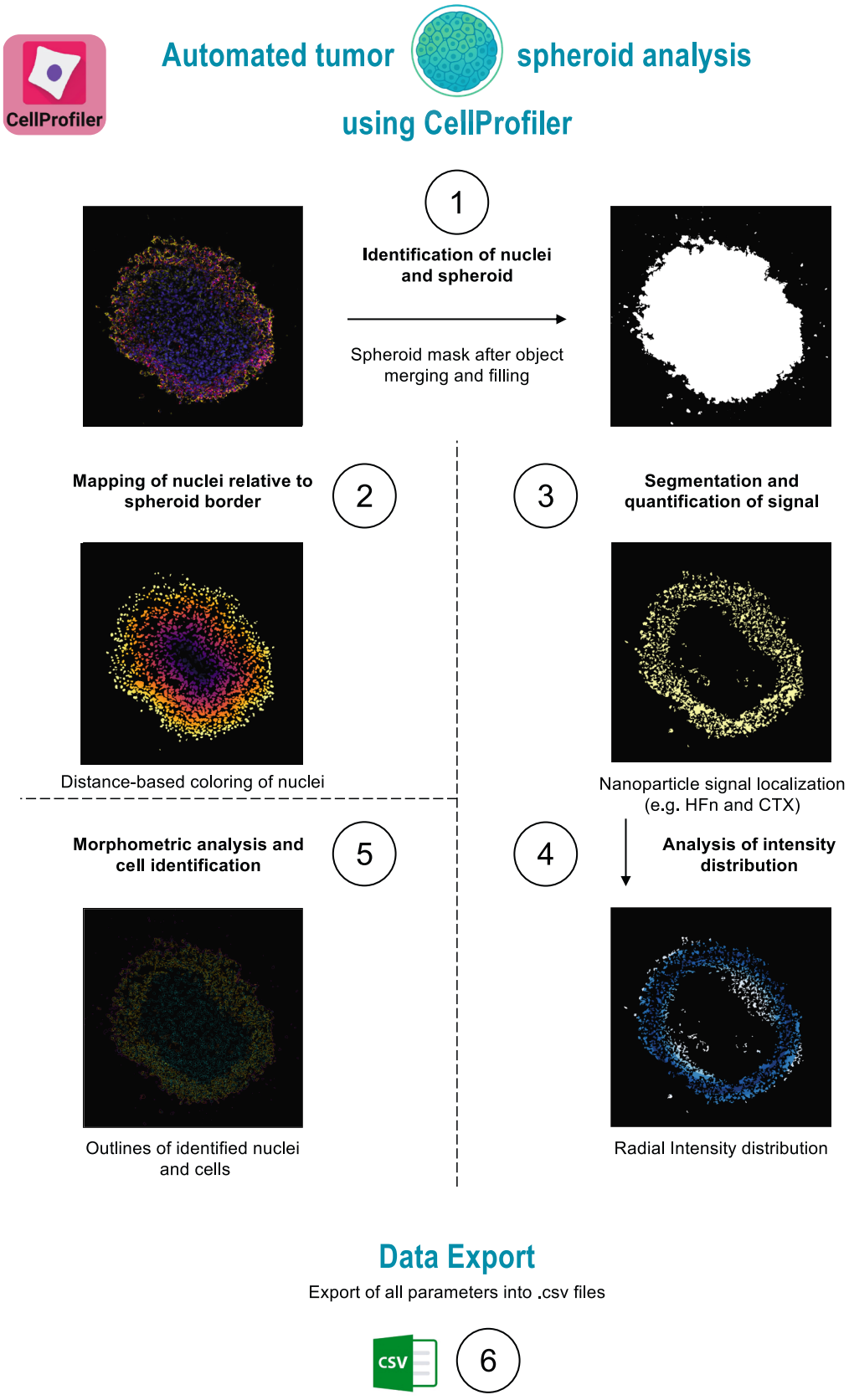

Fig. 5. Automated tumour spheroid analysis workflow in CellProfiler. Stepwise schematic of the image analysis pipeline. Images of spheroid cryosections are processed through sequential modules: (1) identification of nuclei and spheroid objects; (2) merging and filling of spheroid masks; (3) distance-based colouring of nuclei relative to the spheroid border; (4) mapping of nuclei positions and segmentation of nanoparticle fluorescence signals (e.g., HFn and CTX); (5) quantification of morphometric parameters and fluorescence intensities; (6) generation of radial intensity distribution profiles; and (7) export of all measurements to.csv format. The pipeline is semi-automated, requires no coding expertise, and operates efficiently on standard laboratory computers.

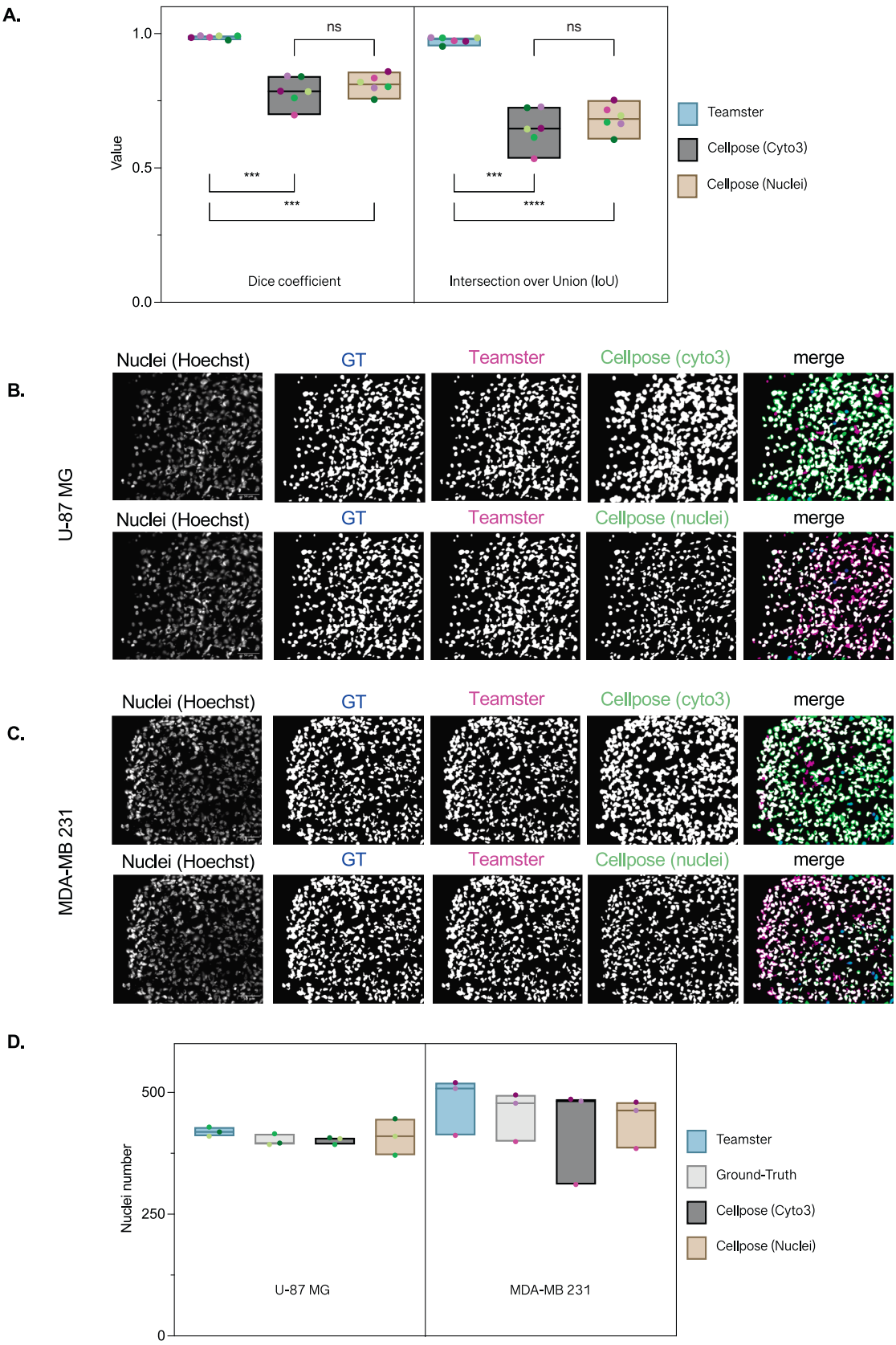

(caption on next page)

Fig. 6. Benchmarking of segmentation accuracy and object-level counting performance of TEAMSTER versus Cellpose-based approaches. (A) Quantitative comparison of segmentation performance using the Dice coefficient and IoU on a benchmark set of six representative cryosection images, including three U-87 MG and three MDA-MB-231 spheroids. Nuclear masks generated by TEAMSTER, the Cellpose Cyto3 model, and the Cellpose nuclei model were compared against manually curated ground-truth annotations. Data are shown as individual coloured dots representing individual images, with median and min–max range. The y-axis indicates the Dice coefficient and IoU, and the x-axis the segmentation method. Statistical significance was assessed by one-way ANOVA followed by Tukey's multiple comparison test (*** $p < 0{,}001$, **** $p < 0.0001$, ns: not significant). (B,C) Representative segmentation outputs for U-87 MG (B) and MDA-MB-231 (C) spheroid cryosections showing nuclei stained with Hoechst, with manually curated ground truth, TEAMSTER segmentation (magenta in merge), Cellpose segmentation masks (cyto3 or nuclei segmentation model, green in merge). (D) Quantitative comparison of identified nuclei. Data are shown as individual coloured dots representing individual images, with median and min–max range. The y-axis indicates the number of detected nuclei across U-87 MG and MDA-MB-231 spheroids, and the x-axis the segmentation method.

incorporating a centrifugation step into the spheroid formation protocol for U-87 MG cells (Fig. 2**A**), we achieved intraplate CVs as low as 4.83% and an interplate CV of 8.9% (Fig. 2**B**), representing a marked improvement over existing method.

We next addressed MDA-MB-231 triple-negative breast cancer cells, which present a particular challenge due to their tendency to form loose and morphologically irregular spheroids, and for which no CV values have previously been reported. An additional optimisation, seeding cells in medium supplemented with Cultrex prior to centrifugation (Fig. 2**A**), enabled us to obtain intraplate and interplate CVs of 3.97-8.69% and 9.4%, respectively (Fig. 2**B**).

3.3. Enhanced cryosectioning efficiency via colour-coded OCT embedding

A few protocols for organoid or spheroid cryosectioning and/or immunostaining have been published, but these have generally focused on selected aspects of sample processing, staining, or imaging rather than integrating robust specimen handling with standardized downstream quantitative analyses. [11–15,21]

We introduced minimally perturbing handling procedures to avoid spheroid shear and deformation, and also modified PFA fixation and the cryopreservation steps to minimize artefacts (Fig. 3**A,** details in the **Supplementary material**). [16,17]

Furthermore, we set out to tackle the long-standing challenge of locating spheroids amid transparent OCT, a major cause for low yields of recovered spheroids. To solve this issue, a common trick is to place a coloured thread near the deposited spheroids. However, this does not always help in locating the spheroid during sectioning, as the thread often shifts before the OCT has solidified or its shredded fibres contaminate the specimen. We devised a colour-coded OCT approach, where alternating layers of pigmented and transparent OCT mark the spheroid plane, enabling easier localization and improved spheroid recovery (Fig. 3**B**).

Although we cut thin sections of only 7 μm to obtain reliable single-cell measurements and morphometric parameters, the TEAMSTER's cryosectioning procedure preserved both the morphology and the integrity of the spheroids while allowing for immunostaining with nuclear, cytosolic, and membrane markers. This could be achieved also for spheroids that are not particularly compact, such as those formed by MDA-MB-231 cells, thanks to our step-by-step protocol (see **Supplementary material**).

3.4. Optimized fixation for high-quality fluorescence staining and imaging

Our immunostaining protocol greatly benefits from fixation [16,17] and dehydration procedures [18] that have been perfected to minimize artifacts while preserving antigenicity and concomitantly reducing background fluorescence. These conditions, along with the inclusion of a high BSA concentration during blocking and all immunostaining steps, enabled multiplexed detection of nanoparticle signals alongside both membrane and cytosolic cellular markers (Fig. 4 and **Supplementary material**). This approach allows the detection of fluorescent signals of variable intensity, as illustrated by AlexaFluor-647-labelled HFn and AlexaFluor-750-labelled CTX in TNBC and glioblastoma spheroids (Fig. 4 and [13]).

3.5. Automated analysis of tumour spheroids and characterization of nanoparticle penetration using CellProfiler

The last step of TEAMSTER leverages a flexible pipeline for high-throughput image analysis that builds on CellProfiler, a user-friendly freeware, to quantify the distribution of fluorescent nanoparticles (or cargoes) inside sectioned spheroids (Fig. 5 and [18]). As a quality control, we performed colocalization analyses within the CellProfiler pipeline by adding modules such as MeasureColocalization, when both signals are reasonably satisfactory, or MeasureObjectOverlap, when one of them is borderline. In this way, we found that reliable measurements could be obtained from both strong fluorescence signals arising from immunostaining with labelled secondary antibodies and weaker signals, such as those generated by fluorescent nanoparticles (not shown and [18]). Hence, the pipeline is robust and supports the analysis of images of variable quality; however, minor parameter adjustments may be required when immunostaining quality, image resolution, or dynamic range differ substantially from those used here. Given the variability in spheroid size, manual curation of the output from the *MeasureObjectIntensityDistribution* module may be required to accurately identify the annulus corresponding to the outer border of each analysed spheroid, which should be designated as annulus 1.

To quantitatively evaluate segmentation performance, we compared nuclear masks generated by TEAMSTER, the Cellpose Cyto3 model, and the Cellpose nuclei model against manually curated ground-truth annotations on a small benchmark set comprising three cryosection images from U-87 MG spheroids and three from MDA-MB-231 spheroids. Segmentation agreement was assessed using the Dice coefficient and intersection-over-union (IoU), which quantify the pixel-wise overlap between predicted and ground-truth masks. We found that TEAMSTER yielded significantly higher Dice and IoU values than both Cellpose-based approaches across the benchmark dataset, whereas no significant difference was detected between the Cellpose nuclei and Cellpose Cyto3 models (Fig. 6**A**). Representative segmentation masks and merged overlays for both U-87 MG and MDA-MB-231 images confirmed the close correspondence between TEAMSTER and the manual ground truth and highlighted the larger deviations observed with the two deep learning-based methods (Fig. 6**B,C**). These metrics provide quantitative support for the robustness and accuracy of TEAMSTER for nuclear segmentation in cryosectioned tumour spheroids.

As an additional object-level validation, we extracted the number of nuclei identified by each method (Fig. 6**D**) and compared them against manual ground-truth counts to assess counting accuracy. Across the six benchmark images, our pipeline showed the lowest overall counting error (mean absolute error, MAE: 20.3 nuclei; mean percent error: 4.7%), compared with the Cellpose Cyto3 segmentation model (MAE: 24.3 nuclei; mean percent error: 6.0%) and the Cellpose nuclei segmentation model (MAE: 25.8 nuclei; mean percent error: 6.2%). However, the two Cellpose-based approaches performed better in a spheroid type-dependent manner, with the Cyto3 model yielding the lowest error in U-87 MG images (MAE: 15.0 nuclei; mean percent error: 3.7%) and the nuclei model performing best in MDA-MB-231 images (MAE: 14.7 nuclei; mean percent error: 3.2%). Notably, TEAMSTER ranked second in both instances, with a MAE of 18.0 nuclei and a mean percent error of 4.5% in U-87 MG images, and a MAE of 22.7 nuclei and a mean percent

Section	Problem	Possible reason	Possible solution
Treatment with the compound	Loss of spheroids during washing	Excessive pipetting	Aspirate medium gently by tilting the plate and placing the pipette on the side. Use a dark background for visibility and collect medium in a tube to recover lost spheroids
Embedding in OCT	"Gel" formation on OCT block	Ethanol contamination; mold submerged too deeply	Avoid sinking the mold in the ethanol/dry ice bath. keep ~1.5 cm depth
	Cracks, fractures, or air bubbles in the block	Slow or uneven freezing; residual sucrose or trapped air	Freeze rapidly using an ethanol/dry ice bath, keeping mold on the surface. Ensure sucrose is fully removed and gently place spheroids with a spatula to avoid air bubbles
	Spheroids deform or collapse in OCT	Harsh pipetting or residual medium	Use a spatula to gently transfer spheroids. Remove excess medium/sucrose before embedding
Cryosectioning	Spheroid not visible during sectioning	Use of transparent OCT or shifted positioning	Use colored OCT layers to mark spheroid position. Avoid threads that can move before solidification. Center spheroids during embedding
	Section breaks, cracks, or block too hard	Cryostat too cold or block not equilibrated	Equilibrate blocks at -20 °C for ≥1 h. Maintain cryostat at -30 °C. If too hard, adjust temperature slightly upwards
	Section defects (lines, scoring, sticking)	Blade damaged or cryostat parts misaligned	Replace microtome blade. Clean and realign antiroll plate
	No spheroids in sections	Spheroid not centered in cutting plane	Use colored OCT for better placement and embed multiple spheroids per block
Staining and Imaging	Autofluorescence or weak signal	Slide overdried; poor fixation or reagent loss	Limit air-drying to 10 min. Use fresh PFA and handle samples in the dark. Minimize exposure to ambient light and over-drying
	Section detaches from slide	Insufficient adherence or improper drying	Use Superfrost Plus slides. Ensure proper drying before staining
	Signal intensity uneven between samples	Variable section thickness or spheroid position	Cut all sections from the same color layer and maintain consistent thickness (e.g., 7 µm)

Fig. 7. Troubleshooting guide for common issues in the TEAMSTER workflow. Overview of typical problems encountered during key steps of the TEAMSTER protocol – compound treatment, OCT embedding, cryosectioning, and staining/imaging – together with likely causes and practical solutions. The table highlights recurring challenges such as spheroid loss during handling, embedding artefacts, sectioning defects, and staining inconsistencies, providing users with actionable recommendations to maximize sample recovery, section integrity, and signal quality.

error of 4.9% in MDA-MB-231 images. These results indicate that TEAMSTER provides robust and comparatively consistent single-cell identification across distinct spheroid morphologies.

Hence, this pipeline lowers barriers to quantitative image analysis, as CellProfiler is entirely GUI-based and can be run on standard laboratory computers without requiring coding expertise, neural network-based models, or advanced computing resources.

4. Discussion

TEAMSTER provides a comprehensive and accessible pipeline for researchers working with 3D tumour spheroids. The workflow begins with a standardised and reproducible spheroid formation protocol, ensuring consistent production of physiologically relevant tumour models that more closely mimic *in vivo* conditions. In addition, the implementation of a layered, colour-coded OCT embedding strategy substantially improves spheroid visibility during cryosectioning,

Feature	Other workflows	TEAMSTER
End-to-end workflow	Fragmented	Integrated
Spheroid benchmarking	Rare	Included
LN_2-free embedding	Rare	Yes
Spheroid localization in OCT	Poor	Colour-coded
Image segmentation benchmarking	Rare	Included
Automated quantification	Often manual	Semi-automated
Coding/machine learning required	Often	No
Special hardware requirements	Yes	No

Fig. 8. Comparison of TEAMSTER with commonly used spheroid analysis workflows. The table summarizes key methodological features of TEAMSTER in comparison with common spheroid-based workflows, highlighting differences in workflow integration, standardization, sample processing, and quantitative image analysis requirements.

addressing a long-standing practical challenge associated with locating spheroids embedded in transparent OCT. This innovation streamlines the cryostat sectioning process, enabling accurate positioning and preservation of spheroid architecture, an essential prerequisite for reliable downstream immunostaining and imaging. In this respect, TEAMSTER complements ongoing efforts in the field. Recently, a whole-mount protocol has expanded the possibilities for staining and automated confocal imaging of intact tumour spheroids, but it depends on compatible confocal instrumentation, limiting its applicability to large spheroids, and dedicated imaging workflows [11]. Section-based approaches, on the other hand, have improved cryosection integrity and antigen retrieval for large and fragile spheroids, thereby facilitating access to internal regions that are difficult to analyse in intact samples [12]. Furthermore, different preparation strategies have been shown to be best suited to prioritize intact morphology, high-quality immunofluorescence, or immunohistochemistry [14].

Building on these optimised sample preparation steps, TEAMSTER integrates a robust and user-friendly CellProfiler pipeline for quantitative image analysis, designed explicitly with accessibility in mind. Deep-learning-based tools, such as the generalist cellular segmentation framework Cellpose3 [22], as well as Python-based multidimensional image viewers for annotation and analysis (e.g., napari), can provide impressive segmentation performance, but they often require complex software environments, command-line interaction, and greater computational resources to run efficiently. These requirements constitute a substantial barrier for laboratories lacking computational infrastructure or bioinformatics expertise. In contrast, CellProfiler is entirely GUI-based and can be executed on standard laboratory computers without the need for coding or advanced hardware. Importantly, our results indicate that TEAMSTER achieves biologically meaningful segmentation and quantification using classical image-processing approaches, without relying on AI- or neural network-based models. This supports the view that learning-based and rule-based workflows are complementary, with TEAMSTER offering a particularly practical solution when transparency, reproducibility, ease of deployment, and accessibility are major priorities.

A key strength of the TEAMSTER CellProfiler pipeline lies in its robustness across a wide range of image qualities and sample heterogeneity. Indeed, the workflow reliably segments and quantifies spheroid sections exhibiting variability in fluorescence intensity, background noise, or morphology. For example, it performs consistently with both compact and irregular spheroids, as well as with sections affected by uneven illumination or partial sectioning. Moreover, because the segmentation modules are not trained on specific datasets, the pipeline avoids dependence on training-set composition and can be adapted to non-standard or previously unseen samples through parameter tuning rather than model retraining. As a result, this workflow is well suited to both novices with no coding skills or access to high-performance computers and advanced users seeking reproducible, transparent, and interpretable quantitative outputs. The workflow can support a broad range of experimental settings, from tissue and spheroid cryosections to multiple imaging modalities, including widefield and confocal microscopy.

Within the rapidly changing landscape of 3D biology, TEAMSTER is positioned as a broadly accessible end-to-end workflow that integrates reproducible spheroid generation, robust cryosection-based processing, multiplex-compatible staining, and downstream quantitative image analysis in a single experimental framework.

When properly implemented (Fig. 7), TEAMSTER functions as an open-source solution for the rapid extraction of single-cell quantitative information from spheroid images, thereby enhancing the objectivity and statistical power of spheroid-based assays. By lowering technical and computational barriers (Fig. 8), TEAMSTER may accelerate wider adoption of quantitative imaging approaches and facilitate data-driven investigations in cancer biology and nanomedicine.

Funding

The research leading to these results has received funding from AIRC under IG 2018 – ID. 21565 project – P.I. D. Prosperi, and Fondazione Cariplo (project # GJC230660) to M. Innocenti. Support to this work was also provided by the European Union – NextGenerationEU through the Italian Ministry of University and Research under PNRR – M4C2-I1.3 Project PE_00000019 “HEAL ITALIA” to D. Prosperi and M. Innocenti CUP H43C22000830006 of University of Milano-Bicocca. The views and opinions expressed are those of the authors only and do not necessarily reflect those of the European Union or the European Commission. Neither the European Union nor the European Commission can be held responsible for them.

Declaration of competing interest

The authors declare that they have no known competing financial interests or personal relationships that could have appeared to influence the work reported in this paper.

Appendix A. Supplementary data

Supplementary data to this article can be found online at https://doi.org/10.1016/j.ymeth.2026.04.015.

Data availability

Data will be made available on request.

References

[1] K. Białkowska, P. Komorowski, M. Bryszewska, K. Miłowska, Spheroids as a Type of Three-Dimensional Cell Cultures-Examples of Methods of Preparation and the Most Important Application, Int J Mol Sci 21 (2020) 6225, https://doi.org/10.3390/ijms21176225.

[2] F. Perche, V.P. Torchilin, Cancer cell spheroids as a model to evaluate chemotherapy protocols, Cancer Biology & Therapy 13 (2012) 1205–1213, https://doi.org/10.4161/cbt.21353.

[3] F. Foglietta, L. Serpe, R. Canaparo, The Effective Combination between 3D Cancer Models and Stimuli-Responsive Nanoscale Drug Delivery Systems, Cells 10 (2021) 3295, https://doi.org/10.3390/cells10123295.

[4] S.A. Langhans, Three-Dimensional in Vitro Cell Culture Models in Drug Discovery and Drug Repositioning, Front Pharmacol 9 (2018) 6, https://doi.org/10.3389/fphar.2018.00006.

[5] R. Edmondson, J.J. Broglie, A.F. Adcock, L. Yang, Three-Dimensional Cell Culture Systems and Their Applications in Drug Discovery and Cell-Based Biosensors, Assay Drug Dev Technol 12 (2014) 207–218, https://doi.org/10.1089/adt.2014.573.

[6] S.-Y. Lee, I.-S. Koo, H.J. Hwang, D.W. Lee, *In Vitro* three-dimensional (3D) cell culture tools for spheroid and organoid models, SLAS Discovery 28 (2023) 119–137, https://doi.org/10.1016/j.slasd.2023.03.006.

[7] P. Boix-Montesinos, P.M. Soriano-Teruel, A. Armiñán, M. Orzáez, M.J. Vicent, The past, present, and future of breast cancer models for nanomedicine development, Adv Drug Deliv Rev 173 (2021) 306–330, https://doi.org/10.1016/j.addr.2021.03.018.

[8] G. Rossi, A. Manfrin, M.P. Lutolf, Progress and potential in organoid research, Nat Rev Genet 19 (2018) 671–687, https://doi.org/10.1038/s41576-018-0051-9.

[9] M. Cangkrama, M. Wietecha, N. Mathis, R. Okumura, L. Ferrarese, D. Al-Nuaimi, M. Antsiferova, R. Dummer, M. Innocenti, S. Werner, A paracrine activin A-mDia2 axis promotes squamous carcinogenesis via fibroblast reprogramming, EMBO Mol Med 12 (2020) e11466, https://doi.org/10.15252/emmm.201911466.

[10] M. Cangkrama, H. Liu, J. Whipman, M. Zubair, M. Matsushita, M. Di Filippo, M. Kopf, M. Innocenti, S. Werner, A Protumorigenic mDia2-MIRO1 Axis Controls Mitochondrial Positioning and Function in Cancer-Associated Fibroblasts, Cancer Res 82 (2022) 3701–3717, https://doi.org/10.1158/0008-5472.CAN-22-0162.

[11] B. Genenger, L. McAlary, J.R. Perry, B. Ashford, M. Ranson, Protocol for the generation and automated confocal imaging of whole multi-cellular tumor spheroids, STAR Protoc 4 (2023) 102331, https://doi.org/10.1016/j.xpro.2023.102331.

[12] C. Charlet-Faure, A.P. Thulesen, A. Rogowska-Wrzesinska, Advancements in 3D spheroid imaging: Optimised cryosectioning and immunostaining techniques, MethodsX 11 (2023) 102415, https://doi.org/10.1016/j.mex.2023.102415.

[13] B. Haspels, M.M.P. Kuijten, Protocol for formation, staining, and imaging of 3D breast cancer models using MicroTissues mold systems, STAR Protoc 5 (2024) 103250, https://doi.org/10.1016/j.xpro.2024.103250.

[14] A. Mondal, S. Nandi, B. Mandal, I. Banerjee, M.W.A. Ddoza Hazari, C. Das, Protocol for 3D tumor spheroid generation, immunostaining, and imaging through comparative approaches, STAR Protoc 6 (2025) 104168. doi:10.1016/j.xpro.2025.104168.

[15] M. Vitacolonna, R. Bruch, R. Schneider, J. Jabs, M. Hafner, M. Reischl, R. Rudolf, A spheroid whole mount drug testing pipeline with machine-learning based image analysis identifies cell-type specific differences in drug efficacy on a single-cell level, BMC Cancer 24 (2024) 1542, https://doi.org/10.1186/s12885-024-13329-9.

[16] D. Leyton-Puig, K.M. Kedziora, T. Isogai, B. van den Broek, K. Jalink, M. Innocenti, PFA fixation enables artifact-free super-resolution imaging of the actin cytoskeleton and associated proteins, Biol Open 5 (2016) 1001–1009, https://doi.org/10.1242/bio.019570.

[17] D. Leyton-Puig, T. Isogai, E. Argenzio, B. van den Broek, J. Klarenbeek, H. Janssen, K. Jalink, M. Innocenti, Flat clathrin lattices are dynamic actin-controlled hubs for clathrin-mediated endocytosis and signalling of specific receptors, Nat Commun 8 (2017) 16068, https://doi.org/10.1038/ncomms16068.

[18] L. Barbieri, L. Salvioni, A. Banfi, S. Garbujo, L. Fiandra, C. Baioni, M. Giustra, L. Morelli, G. Frascotti, M. Colombo, M. Innocenti, D. Prosperi, Dual-Targeting Strategy to Repurpose Cetuximab with HFn Nanoconjugates for Immunotherapy of Triple-Negative Breast Cancer, ACS Appl. Mater. Interfaces (2025), https://doi.org/10.1021/acsami.5c06626.

[19] D.R. Stirling, M.J. Swain-Bowden, A.M. Lucas, A.E. Carpenter, B.A. Cimini, A. Goodman, CellProfiler 4: improvements in speed, utility and usability, BMC Bioinformatics 22 (2021) 433, https://doi.org/10.1186/s12859-021-04344-9.

[20] M. Vinci, S. Gowan, F. Boxall, L. Patterson, M. Zimmermann, W. Court, C. Lomas, M. Mendiola, D. Hardisson, S.A. Eccles, Advances in establishment and analysis of three-dimensional tumor spheroid-based functional assays for target validation and drug evaluation, BMC Biology 10 (2012) 29, https://doi.org/10.1186/1741-7007-10-29.

[21] L.-B. Weiswald, J.-M. Guinebretière, S. Richon, D. Bellet, B. Saubaméa, V. Dangles-Marie, In situ protein expression in tumour spheres: development of an immunostaining protocol for confocal microscopy, BMC Cancer 10 (2010) 106, https://doi.org/10.1186/1471-2407-10-106.

[22] C. Stringer, M. Pachitariu, Cellpose3: one-click image restoration for improved cellular segmentation, Nat Methods 22 (2025) 592–599, https://doi.org/10.1038/s41592-025-02595-5.